Front. Phys., 2012, 7(2): 208–217
DOI 10.1007/s11467-011-0199-7

REVIEW ARTICLE

Topological insulator nanostructures: Materials synthesis, Raman spectroscopy, and transport properties

Hui Li (李辉), **Hailin Peng** (彭海琳)*, **Wenhui Dang** (党文辉), **Lili Yu** (余力立), **Zhongfan Liu** (刘忠范)†

Center for Nanochemistry, Beijing National Laboratory for Molecular Sciences (BNLMS), State Key Laboratory for Structural Chemistry of Unstable and Stable Species, College of Chemistry and Molecular Engineering, Peking University, Beijing 100871, China

*E-mail: *hlpeng@pku.edu.cn, †zfliu@pku.edu.cn*

Received June 27, 2011; accepted August 16, 2011

Nanostructured topological insulator materials such as ultrathin films, nanoplates, nanowires, and nanoribbons are attracting much attention for fundamental research as well as potential applications in low-energy dissipation electronics, spintronics, thermoelectrics, magnetoelectrics, and quantum computing due to their extremely large surface-to-volume ratios and exotic metallic edge/surface states. Layered Bi_2Se_3 and Bi_2Te_3 serve as reference topological insulator materials with a large nontrivial bulk gap up to 0.3 eV (equivalent to 3600 K) and simple single-Dirac-cone surface states. In this mini-review, we present an overview of recent advances in nanostructured topological insulator Bi_2Se_3 and Bi_3Te_3 from the viewpoints of controlled synthesis and physical properties. We summarize our recent achievements in the vapor-phase synthesis and structural characterization of nanostructured topological insulator Bi_2Se_3 and Bi_2Te_3, such as nanoribbons and ultrathin nanoplates. We also demonstrate the evolution of Raman spectra with the number of few-layer topological insulators, as well as the transport measurements that have succeeded in accessing the surface conductance and surface state manipulations in the device of topological insulator nanostructures.

Keywords topological insulator, nanostructure, synthesis, Raman, transport, surface state manipulation

PACS numbers 73.20.-r, 68.65.-k, 74.25.nd

Contents

1 Introduction

Stoichiometric compounds Bi_2Se_3, Bi_2Te_3, and Sb_2Te_3 are predicted to be three-dimensional (3D) topological insulators (TIs) with an insulating bulk state and robust surface states consisting of a single Dirac cone at the Γ point [1]. Among these compounds, Bi_2Se_3 is found to have a large nontrivial bulk gap of about 0.3 eV (equivalent to 3600 K), making it an attractive reference material for exploring the physical properties of the topological surface states [1, 2]. The Dirac-cone surface states of 3D TIs have been mainly investigated by angle-resolved photoemission spectroscopy (ARPES) and scanning tunneling microscopy (STM) [3–6]. These studies have focused mainly on cleaved surface of bulk crystals grown by self-flux method [7]. However, TI bulk crystals are unintentionally and uncontrollably doped by anion vacancies

and anti-sites defects, which give rise to the presence of large bulk electron pockets near the Fermi level in these samples. As a result, it is difficult to probe the transport properties and manipulate topological surface states in bulk crystal samples because the surface states are significantly overwhelmed by the unwanted bulk carriers [6, 8, 9].

It is desirable to find effective and convenient methods to obtain true TI samples with the Fermi level lying in the bulk gap, suitable for studying the transport properties of surface states. The material quality of TI bulk crystals can be further improved by compensating the anion vacancies or reducing the defects via an annealing process in excess of Se or Te. However, this is challenging due to the high volatility of Se and Te. Doping the bulk crystals with elements such as Sn, Ca, Sb or Pb can also effectively tune the Fermi level into the bulk gap [4, 5, 10–12], but this method usually carries the caveat of lowering the crystalline quality and carrier mobility. Chemical doping can also tune the Fermi level in TIs by adsorbing NO_2 molecules on the surface of Bi_2Se_3 crystal [7], although such a technique may be incompatible with device fabrication processes since NO_2 is not the most user-friendly gas and easily desorbs from the surface.

Compared with bulk materials, TI nanostructures with large surface-to-volume ratios such as thin films, nanoplates, nanowires, and nanoribbons are expected to significantly enhance topological surface conduction, and can also facilitate external manipulation of the surface states. Furthermore, TI nanostructures can provide excellent geometries for investigating the transport properties of exotic surface states. In particular, quasi-two-dimensional (quasi-2D) nanoribbons, nanoplates, and thin films of TIs may have superior applications in electronic devices because it is relatively easy to fabricate complex structures from them.

Recently, we have demonstrated direct transport evidence of the robust, conducting surface states in TI nanoribbons. In the initial work, pronounced Aharonov–Bohm oscillations have been observed in Bi_2Se_3 nanoribbons, which present the first demonstration of quantum interference in the transport properties of TIs [13]. Following this work, the Kondo effect has also been revealed below ~30 K in magnetically-doped Bi_2Se_3 nanoribbons [14]. Several groups have demonstrated that the surface states of TI nanostructures can be easily manipulated by an external electric field [15–19]. For example, in Bi_2Te_3 nanoplates, we observed a clear gate effect and tunable chemical potential by the combination of a strong electrical field from the top gate using a high-k dielectric layer and ultrathin thickness of nanoplates [17]. More recently, Shubnikov–de Haas (SdH) oscillations [15], surface ambipolar effects [16], and weak antilocalization behavior [18] have been observed in electric-field-modulated TIs nanostructures, attractive for probing topological surface states and future device applications.

In this mini-review, we present the recent progress in the controlled synthesis, structural characterizations, Raman spectroscopy, and transport measurements of TI nanostructures. We first summarize the recent advances in the production of TI nanostructures. Then we give Raman characterizations of TI nanostructures. Finally, we present studies on the transport properties of surface conductance and surface state manipulations in TI nanostructure devices.

2 Results and discussion

2.1 Production of TI nanostructures

To date, controlled production of TI nanostructures with high crystalline quality and high carrier mobility is still lacking. Layered Bi_2X_3 (X = Se, Te), the reference TIs, share the same rhombohedral crystal structure in the space group $D_{3d}^5(R\bar{3}m)$, with each quintuple layer (QL) consisting of X–Bi–X–Bi–X sheets. The planar, covalently bonded sheets are held together by weak van der Waals interactions [Fig. 1(a)]. Bulk materials of Bi_2X_3 usually exist in the layered form of quasi-2D flakes or platelets owing to this anisotropic bonding. On the other hand, the anisotropic bonding characteristics may play an important role in the production of TI nanostructures.

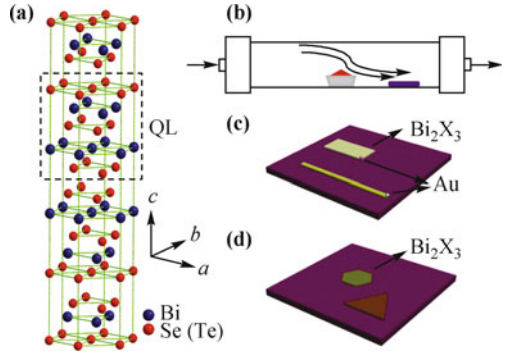

Fig. 1 **(a)** Crystal structure of layered Bi_2X_3 (X = Se, Te). A dashed dark box indicates the X–Bi–X–Bi–X quintuple layer (QL). Each QL, with thickness of 9.55 Å for Bi_2Se_3 and 10.17 Å for Bi_2Te_3, is composed of covalently bonded sheets ordered in X–Bi–X–Bi–X sequence along the c axis. **(b)** A schematic drawing of the growth process for nanostructures of Bi_2X_3 in a horizontal tube furnace. **(c, d)** Schematic drawings of the growth mechanism for quasi-1D and quasi-2D nanostructures, respectively.

Various methods have been used to produce Bi_2X_3 nanostructures, which can be generally classified into "bottom–up" and "top–down" approaches. The "top–down" approach includes micromechanical exfoliation by scotch tape [20, 21], peeling with an AFM tip [22], and chemical exfoliations [23] of few-layer Bi_2X_3 sheets from bulk crystal samples. This simple micromechanical exfoliation has been used to yield high quality, isolated nanosheets [21]. However, this method still has some lim-

itations such as low yield, irregular shapes, and poor controllability. In the "bottom–up" approach, few-layer Bi_2X_3 are synthesized from atoms or molecules via chemical reactions. Chemical vapor transport [13, 24], metal-organic chemical vapor deposition [25], molecular beam epitaxy (MBE) [26, 27], and wet chemical synthesis [28, 29] are some prominent examples of the "bottom-up" approach. MBE is a promising technique to grow high-quality TI films in a very controlled manner. Ultrathin films of TIs down to 1 QL were obtained by MBE [12, 26, 30], and Landau quantization of the topological surface states was observed in these high-quality films [31]. However, the state-of-art MBE technique is expensive with limited accessibility.

We have developed facile vapor-phase deposition methods to grow TI nanostructures with high crystallinity and diverse morphologies [13, 24, 32]. Quasi-1D nanowires and nanoribbons have been synthesized via a catalyst-assisted vapor–liquid–solid (VLS) growth. Ultrathin quasi-2D nanoplates of Bi_2Se_3 and Bi_2Te_3 with uniform thickness down to one QL and the lateral dimensions up to 100 μm have been grown via van der Waals epitaxy.

2.1.1 Synthesis of Quasi-1D nanostructures of TIs

VLS growth has proven to be an effective method to obtain quasi-1D nanostructures with high crystalline quality and clean surfaces [33–40]. We synthesized high-quality Bi_2Se_3 nanowires and nanoribbons by means of a gold-catalyzed VLS growth [13, 24]. The schematic diagram of the growth system is shown in Figs. 1(b) and (c).

Scanning electron microscope (SEM) images of as-grown quasi-1D nanostructures of Bi_2Se_3 with various morphologies are shown in Fig. 2. We found that morphologies of Bi_2Se_3 nanostructures were controlled by the growth temperature and gas flow rate. Narrow nanoribbons were the dominant products when the substrate temperature was about 450 °C [Fig. 2(a)]. Nanoribbons with various morphologies were obtained when the substrate temperature were about 375 °C, as shown in Fig. 2(b). The growth rate of synthesized products increased dramatically with the increase in source temperature and flow rate. Wide nanoribbons with lateral dimensions of several tens of microns were obtained by using higher source temperature and flow rate [Fig. 2(c)]. We have also observed quasi-1D nanostructures with other diverse morphologies, such as nanowires formed from stacked nanoplates grown along the *c*-axis [Figs. 2(d) and (e)], nanowires grown off along the *c*−axis [Fig. 2(f)], zig-zag nanoribbons [Fig. 2(g)], sheet-like wide nanoribbons [Fig. 2(h)], and nanoplates grown on the substrate via catalyst-free vapor-solid (VS) mechanism [Fig. 2(i)]. High-resolution transmission electron microscope (HRTEM), selected area electron diffraction (SAED), and energy-dispersive X-ray spectroscopy (EDX) studies were used to evaluate the structure and chemical composition of the as-grown quasi-1D nanostructures. Extensive HRTEM and SAED studies have confirmed that the quasi-1D nanostructures have single-crystalline phases with atomically smooth surface/edges. EDX analyses have revealed uniform chemical composition of the TI nanostructures with a Bi: Se atomic ratio of 2:3, indicating stoichiometric Bi_2Se_3 free of detectable impurities within the sensitivity of the EDX analyses (<2%) [13, 24].

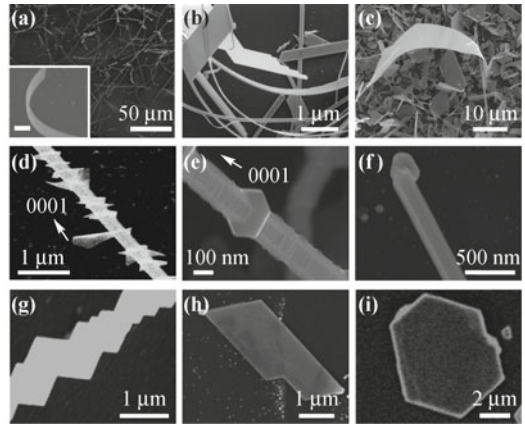

Fig. 2 Typical SEM images of synthesized quasi-1D Bi_2Se_3 nanostructures. **(a)** Nanowires grown on the substrate at about 450 °C. **(b)** Nanoribbons grown on the substrate temperature at about 375 °C. The growth conditions for (a, b): source temperature = 500 °C, Ar flow rate = 100 sccm, growth time = 2 hours, pressure = 20 torr. **(c)** Large nanoribbons obtained with the grown conditions: source temperature = 520 °C, Ar flow rate = 150 sccm, Ar growth time = 2 hours. **(d, e)** Nanowires grown along the *c*−axis. **(f)** Nanowire grown off of the *c*-axis. **(g)** Zig-zag nanoribbon. **(h)** sheet-like wide nanoribbon. **(i)** Nanoplate grown on the substrate by VS mechanism.

2.1.2 Synthesis of Quasi-2D nanostructures of TIs

Van der Waals epitaxy (VDWE) is an effective strategy for growing designed structures of quasi-2D layered materials with van der Waals gaps onto a substrate without surface dangling bonds [41, 42]. In layered TI Bi_2X_3, low surface energy and the absence of unsaturated chemical bonds at the surface can relax stringent lattice matching conditions, which facilitate the growth of high-quality quasi-2D nanostructures of TIs on various substrates such as oxidized silicon [17], graphene [32], Si(111) [43], and $SrTiO_3$ [18].

We have achieved the growth of ultrathin Bi_2Se_3 and Bi_2Te_3 nanoplates via a catalyst-free VS process on an oxidized silicon substrate [17]. A diagram for the growth system is shown in Figs. 1(b) and (d). Triangular and hexagonal quasi-2D Bi_2Se_3 and Bi_2Te_3 nanoplates with thicknesses down to ∼3 nm (3 QLs) and lateral dimensions up to 20 microns have been obtained on 300 nm SiO_2/Si substrates with a quasi-VDWE method [Fig.

3(a)] [17]. Most of the nanoplates have a flat surface with uniform lateral thickness. Analyses of the thickness distribution indicated that the major nanoplate products have the thicknesses between 3 QLs and 6 QLs [Figs. 3(b) and (c)]. HRTEM and SAED results revealed the single crystalline nature of the Bi_2Se_3 and Bi_2Te_3 nanoplates. Both Bi_2Se_3 and Bi_2Te_3 nanoplates had (0001) facets as top and bottom surfaces, and (01-10) facets as side surfaces. EDX analyses confirmed the uniform chemical composition of the nanoplates with a Bi: (Se, Te) atomic ratio of 2:3. In addition, we have speculated on the growth mechanism of ultrathin nanoplates on SiO_2/Si substrates. The high anisotropic bonding nature of Bi_2Se_3 and Bi_2Te_3 is believed to play a major role in the growth of ultrathin nanoplates. The growth anisotropy factor is several thousand, estimated by taking the ratio of the lateral to vertical dimensions. The direct growth of ultrathin TI nanoplates onto SiO_2/Si substrates facilitates device fabrications and transport measurements.

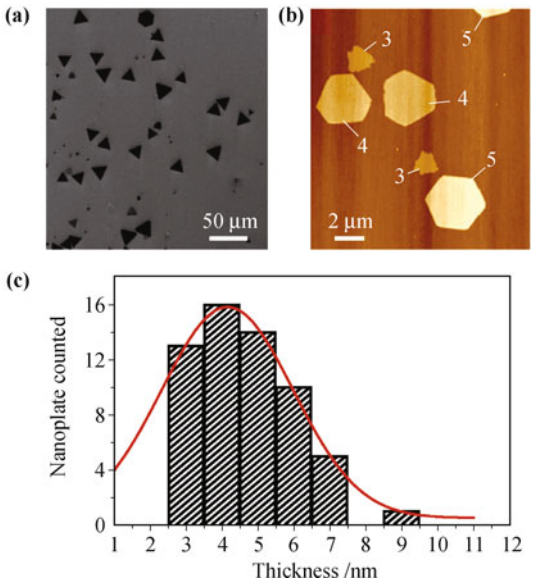

Fig. 3 Vapor-phase synthesis of Bi_2Te_3 nanoplates on an oxidized silicon substrate via quasi-VDWE mode. **(a)** Typical SEM image of Bi_2Te_3 nanoplates. Most nanoplates exhibit triangular and hexagonal morphologies. **(b)** AFM image of several ultrathin Bi_2Te_3 nanoplates. Numbers indicate the number of QLs. **(c)** Thickness distribution histogram of Bi_2Te_3 nanoplates obtained from substrate area of $\sim$ 200 μm^2. The smooth curve is a Gaussian fit to the thickness distribution. Reproduced from Ref. [17], Copyright © 2010 American Chemical Society.

However, the growth of large-area, ultrathin nanoplate/sheets was restricted by the presence of the surface dangling bonds on the SiO_2/Si substrate. In contrast, a layered, chemically inert substrate favors the growth of large-area and high-quality epitaxial layers via the VDWE process. Wu *et al.* has pioneered quintuple-layer epitaxy of TI Bi_2Se_3 thin films on a Si(111) substrate in an MBE apparatus [44]. Following this work, Xie *et al.* has achieved the VDWE of large-area high-quality TI Bi_2Se_3 epifilms on a vicinal Si(111) substrate with the surface dangling bonds saturated by hydrogen atoms [43]. The crystalline Bi_2Se_3 thin films have a low-temperature resistivity of $\sim$1 mΩ cm, a carrier mobility of $\sim$ 2000 $cm^2 \cdot V^{-1} \cdot s^{-1}$, and an electron density of $\sim$ 3×10^{18} cm^{-3}. Recently, Wu *et al.* have achieved high quality, gate-tunable Bi_2Se_3 thin films on SrTiO3 substrates by MBE [18, 19]. Meanwhile, Xue group have succeeded in the growth of high-quality ultrathin TI Bi_2Se_3 films on a graphitized-terminated 6H-SiC (0001) substrate using MBE [26]. Landau quantization in such high-quality Bi_2Se_3 thin films was directly observed by STM [31]. In addition, the same group have reported major achievements on the epitaxy of high-quality Bi_2Te_3 film on Si(111) substrate using MBE [27, 30].

Following our initial work on vapor-phase epitaxy of Bi_2Se_3 and Bi_2Te_3 nanoplates grown on an oxidized silicon substrate [17], we have extended this epitaxy method to the growth of large-area, high crystalline TI nanoplates on VDWE substrates including graphene [32]. Arrays of Bi_2Se_3 and Bi_2Te_3 nanoplates with good orientations were also obtained. More importantly, lateral dimensions of single nanoplates of Bi_2Se_3 and Bi_2Te_3 on the VDWE substrate can reach up to $\sim$0.1 mm. The high quality nanoplates with large lateral dimensions epitaxially grown on an insulating VDWE substrate provided a straightforward platform for spectroscopic characterizations, device fabrications, and transport measurements. Electrodes can be easily patterned on individual nanoplates using standard micro-photolithography techniques. The combination of spectroscopic characterizations with electrical transport measurements allowed us to correlate directly the electrical properties and the structure of the same individual nanoplate (unpublished data).

2.1.3 Epitaxial heterostructure of TI nanoplate and graphene

Graphene, a 2D material consisting of a flat and flexible monolayer of carbon atoms without surface dangling bonds [45, 46], is an excellent VDWE substrate that favors the epitaxial growth of large-area, ultrathin TI nanoplates/sheets. Recently, we have achieved epitaxial heterostructures of ultrathin TI nanoplate and graphene using a simple vapor-phase deposition method [32]. The hexagonal periodicity of graphene surface has a lattice mismatch of $\sim$2.9% with Bi_2Se_3 [Fig. 4(a)]. However, lattice matching conditions can be relaxed drastically in VDWE, allowing the formation of a large variety of high-quality heterostructures [41, 42].

Optical photographs and SEM images of Bi_2Se_3 nanoplates epitaxially grown on a graphene substrate show that the Bi_2Se_3 nanoplates have regular triangular or hexagonal shapes [Figs. 4(b) and (c)]. The lateral

dimension of the nanoplates were in the range of several hundred nanometers to several microns. Each nanoplate has uniform color contrast, suggesting a uniform thickness through the whole nanoplate surface. The Bi_2Se_3 nanoplates were aligned in the same orientation on the graphene substrate. From the histogram of edge orientation distribution shown in Fig. 4(d), the orientation of the nanoplates' edges occur at multiples of 60°, suggesting the epitaxial nature of the growth mechanism.

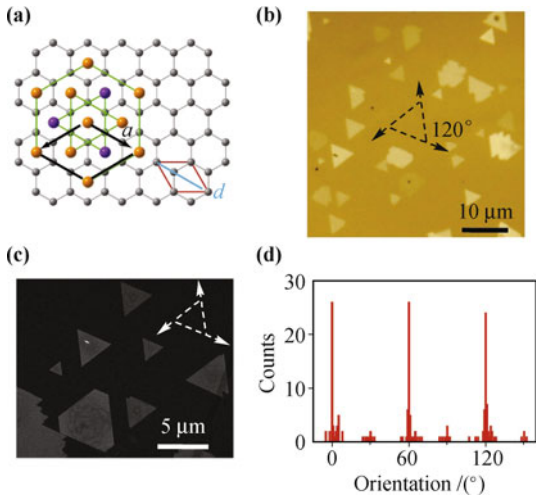

Fig. 4 Vapor-phase synthesis of Bi_2Se_3 nanoplates on few-layer graphene substrates via VDWE. **(a)** Schematic for epitaxial growth mode. **(b)** Typical photograph of Bi_2Se_3 nanoplates epitaxially grown on a multilayer graphene substrate. **(c)** SEM image of triangular or hexagonal nanoplates with the same orientation. **(d)** Orientation distribution histogram of triangular/hexagonal nanoplates. Reproduced from Ref. [32], Copyright © 2010 American Chemical Society.

It is worth noting that the thickness of single crystalline Bi_2Se_3 nanoplates can be as small as 1 QL on pristine graphene substrates. As shown in Fig. 5, continuous, ultrathin Bi_2Se_3 nanoplates with uniform

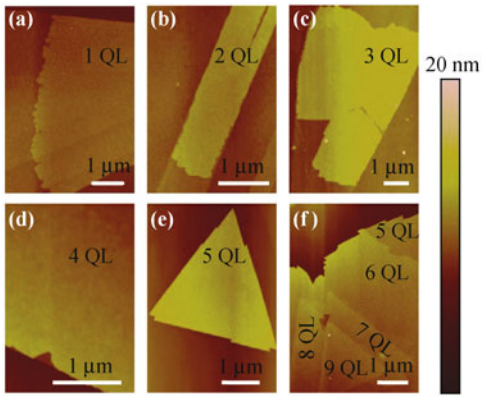

Fig. 5 AFM images of ultrathin Bi_2Se_3 nanoplates with different thicknesses grown on few-layer graphene. **(a)** 1-QL Bi_2Se_3 nanoplate on bilayer graphene; **(b)** 2-QL Bi_2Se_3 nanoplate on bilayer graphene; **(c)** 3-QL Bi_2Se_3 nanoplate on monolayer graphene; **(d)** 4-QL Bi_2Se_3 nanoplate on 3-layer graphene; **(e)** 5-QL Bi_2Se_3 nanoplate on few-layer graphene; **(f)** Layered Bi_2Se_3 nanoplates (5–9 QLs) on few-layer graphene. Reproduced from Ref. [32], Copyright © 2010 American Chemical Society.

thicknesses from 1 QL to 9 QLs epitaxially grown on graphene substrates were characterized by AFM. The atomically flat Bi_2Se_3 nanoplates can grow over the steps of graphene. The size of the Bi_2Se_3 nanoplates greatly depends on the lateral dimension of the graphene substrate since the growth terminates at the edges of graphene.

The structure and chemical compositions of the Bi_2Se_3 nanoplates have been studied by TEM and EDX. EDX revealed the uniform composition of the nanoplate with an exact Bi:Se atomic ratio of 2:3. A typical bright-field TEM image of the triangle Bi_2Se_3 nanoplates with the same orientation epitaxially grown on graphene is shown in Fig. 6(a). A HRTEM image [Fig. 6(b)] and the corresponding SAED pattern [Fig. 6(c)] confirmed the single crystalline nature of the nanoplates. The HRTEM image revealed the expected hexagonal lattice fringes, with a lattice spacing of 0.21 nm, consistent with the lattice spacing of Bi_2Se_3 (11–20) planes [13, 24]. Nanoplates have (0001) facets as top and bottom surfaces, and (01–10) facets as side surfaces.

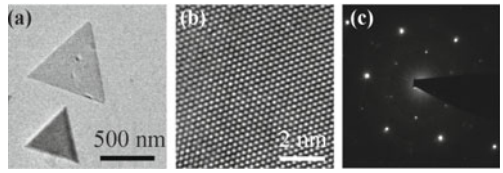

Fig. 6 **(a)** Bright-field TEM image of ultrathin Bi_2Se_3 nanoplates epitaxially grown on few-layer graphene. **(b)** HRTEM image of the ultrathin Bi_2Se_3 nanoplate. **(c)** Corresponding SAED pattern.

Interestingly, Moiré-type modulation structures have been observed in the epitaxial heterostructures of Bi_2Se_3 nanoplates and graphene. In principle, a moiré pattern can be induced by the superposition of the epifilm and substrate due to the lattice mismatch and/or different orientations, which is a useful tool for characterizing interfacial structures and strain development in lattice mismatched semiconductor heterostructures [47, 48]. Take Bi_2Se_3/graphene nanoplate heterostructures for example, Fig. 7(a) shows the planar-view TEM image of two triangular Bi_2Se_3 nanoplates on suspended few-layer graphene membrane recorded along the 0001 zone axis. From the close-up view [Fig. 7(b)], the sets of intersecting translational moiré fringes can be clearly observed in the three main directions ⟨11-20⟩. The well-defined moiré pattern in the left and right nanoplate has a period of about 4.2 and 5.5 nm, respectively [Fig. 7(c)]. The period difference presumably originates from different orientation angles between the Bi_2Se_3 nanoplates and underlying graphene. The highly ordered, defect-free moiré patterns throughout the nanoplates indicate that the Bi_2Se_3 nanoplate has high crystalline quality.

Moiré patterns can be used to determine the plastic relaxation in individual nanoplates. For example, planar-view TEM images of the Bi_2Se_3/graphene nanoplate

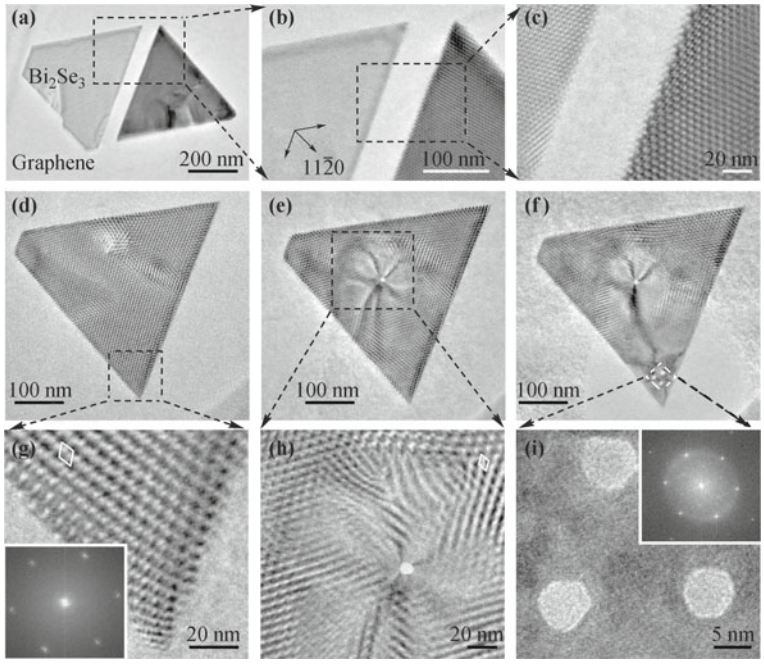

Fig. 7 Moiré patterns of the ultrathin Bi_2Se_3 nanoplates and graphene. **(a)** Typical intersecting translational Moiré fringes pattern along the three main directions ⟨11-20⟩. **(b, c)** Magnified Moiré fringes of the black square in the corresponding bright-field TEM image. **(d)** Moiré patterns of a Bi_2Se_3/graphene nanoplate heterostructure before peeling the graphene. **(e)** TEM image of the Bi_2Se_3/graphene nanoplate heterostructure after peeling the graphene in the black square zones. **(f)** Nanoholes fabricated in the Bi_2Se_3 nanoplates. **(g, h, i)** Magnified image of the square region in the corresponding TEM image (d, e, f), respectively. Down inset and upper inset of (g) and (i) show the corresponding FFT patterns, respectively.

heterostructure [Figs. 7(d) and (g)] reveal a typical highly ordered and continuous moiré pattern with a period of ∼7.3 nm, consistent with the period of the simulated moiré pattern by assuming a fully relaxed Bi_2Se_3 on graphene with a rotational angle of 29° [49]. The corresponding FFT image [inset of Fig. 7(g)] shows two sets of hexagonal spots with a rotational angle, which confirms that the moiré pattern results from the superposition of two structures with different lattice constants and/or orientations. Interestingly, the few-layer Bi_2Se_3 nanoplate are relatively more stable than few-layer graphene against the electron-beam irradiation in a TEM operated at 300 kV. We have carried out layer-by-layer peeling for Bi_2Se_3/graphene nanoplate heterostructures using high-energy electron irradiation. The suspended graphene substrate was first removed by high-energy electron irradiation until a nanometer-sized hole formed in the graphene sheet. The moiré pattern of Bi_2Se_3 nanoplate disappears in the hole region [Figs. 7(e) and (f)], which indicates that the moiré pattern results from the superposition of Bi_2Se_3 and graphene. HRTEM images of the suspended Bi_2Se_3 layer reveal a simple hexagonal lattice of Bi_2Se_3 [Figs. 7(h) and (i)]. The corresponding FFT image [inset of Fig. 7(i)] shows a single diffraction pattern, indicating the disappearance of the moiré pattern and the plastic relaxation in the individual nanoplates.

Another interesting observation was that a high-resolution nanofabrication of TI nanoplates with the help of a high energy, highly focused electron beam has been achieved. As shown in Figs. 7(e) and (f), extremely small nanoholes, as small as 5 nm in diameter, was reproducibly fabricated in TI nanoplates. From the HRTEM images, the holes have a quasi-hexagonal shape with atomically smooth edges [Figs. 7(h) and (i)]. Furthermore, the TEM images recorded near the edges of the nanoholes in the nanoplate display strain contrast presumably induced by corrugating or bending of the suspended nanoplates.

2.2 Raman characterizations of TI nanostructures

Investigations on phonons and electron–phonon interactions in topological insulators, especially down to a few-layer regime, are interesting topics. Raman scattering spectroscopy is a powerful and sensitive tool for the study of phonons in 2D nanomaterials [32, 50], such as graphene and few-layer TIs. We have systemically studied the relationship between Raman spectra and layer numbers of 2D Bi_2Se_3 nanoplates at room temperature in the backscattering geometry [32]. The Raman intensity and frequency shifts have a close relationship with the layer number of TI. Take Bi_2Se_3 nanoplates epitaxially grown on graphene, for example, the layer number of Bi_2Se_3 nanoplates was first identified by optical color contrast [Fig. 8(a)] and confirmed by AFM measurements. Figure 8(b) shows the evolution of Raman spectra produced from a 633 nm laser with the number of Bi_2Se_3 layers. The in-plane vibrational mode (E_g^2) and out-of-plane vibrational mode (A_{1g}^2) of Se–Bi–Se–Bi–Se

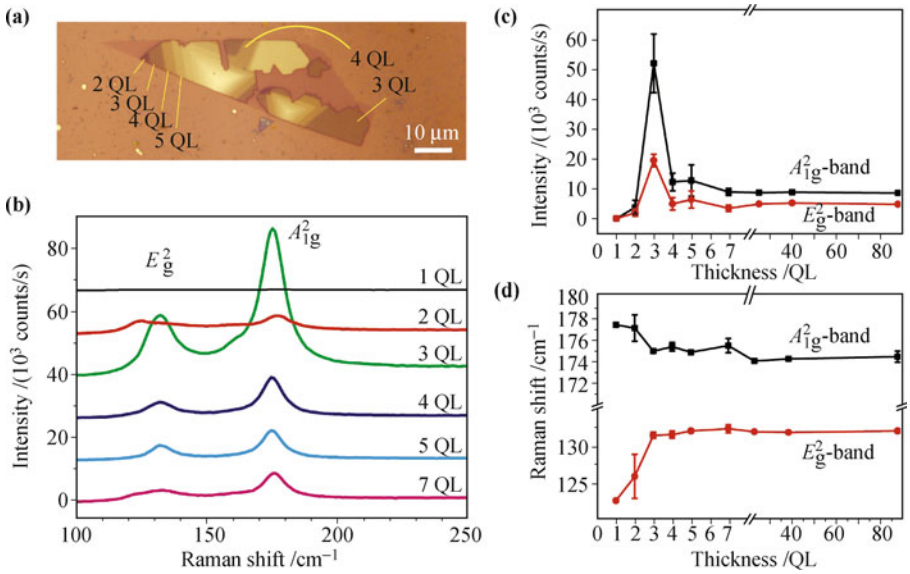

Fig. 8 Raman characterizations of few-layer TI nanostructures. **(a)** Optical image of layered Bi_2Se_3 nanoplates with obvious contrast grown on a graphene substrate. **(b)** Evolution of the Raman spectra at 633 nm laser with the number of Bi_2Se_3 QLs. **(c)** Intensity variation of A_{1g}^2 and E_g^2 bands for Bi_2Se_3 nanoplates as a function of thickness. The 3-QL films have the strongest Raman signals. **(d)** Evolution of the Raman frequency position with the number of layers. Reproduced from Ref. [32], Copyright © 2010 American Chemical Society.

lattice vibration modes [51] were detected at ∼131 and ∼174 cm^{-1}, respectively. Figure 8(c) shows the dependence of the E_g^2 and A_{1g}^2 vibration peaks intensity on the layer number. Bi_2Se_3 nanoplates with a thickness of 3 QLs exhibit the strongest Raman intensity, presumably due to the presence of an enhancement factor.

Strain effects in the Bi_2Se_3/graphene nanoplate heterostructures have also been studied by Raman spectroscopy [32]. Figure 8(d) plots the evolution of the Raman frequency position of the E_g^2 and A_{1g}^2 modes with the number of layers. Both single-QL and 2-QL nanoplates reveal a significant down shift in frequency of the E_g^2 modes, and an upward shift for the frequency of A_{1g}^2 modes. These results suggest that a tensile stress and a compressive stress exist in the *ab*-plane and along the *c*-axis direction of Bi_2Se_3 nanoplates due to lattice mismatch, respectively [52–56]. Meanwhile, the tensile stress of Bi_2Se_3 nanoplates might lead to a compressive stress in the few-layer graphene substrate. Indeed, upward shifts of 4∼10 cm^{-1} for the G-band and 15 ∼ 25 cm^{-1} for 2D-band of graphene were observed, indicating the presence of the compressive stress in the decorated single-layer graphene substrate, consistent with tensile stress in the 1-QL and 2-QL Bi_2Se_3 nanoplates. In contrast, no obvious shifts of Raman position for multilayer (⩾3 QLs) Bi_2Se_3 nanoplates were detected, indicating that the stress inside the multilayer Bi_2Se_3 epifilm was relaxed [52, 56].

2.3 Transport measurements

Quasi-1D and quasi-2D nanostructures of TI Bi_2Se_3, with their large surface-to-volume ratios, provide excellent geometries for manipulating and probing the transport properties of surface states [13, 15, 17, 18]. We have performed transport measurements of TI nanostructures grown by the vapor-phase deposition method [13]. Pronounced Aharonov–Bohm (AB) oscillations associated with the robust topological surface states in Bi_2Se_3 nanoribbons have been observed, which is the first demonstration of quantum interference in the transport properties of TIs [13].

To observe the quantum oscillations caused by the AB effect [Fig. 9(a)], an external magnetic field (B) was applied along the Bi_2Se_3 nanoribbon length [Fig. 9(b)]. Four-point probe devices have been fabricated by depositing Ti/Au ohmic contacts onto the nanoribbon [Fig. 9(b)]. For the 2D states covering the entire surface, the TI nanoribbon can be considered as a hollow conducting cylinder. Owing to the quantum interference effect, the magnetoconductance depends on the magnetic flux enclosed by the cylinder and oscillates with a period given by the magnetic flux quantum h/e, where h is Planck's constant and e is the elementary charge. The weak anti-localization effect characterized by a sharp cusp was observed at low magnetic fields, indicating the presence of the strong spin–orbit coupling in Bi_2Se_3 nanoribbons [Fig. 9(c)]. Pronounced and reproducible resistance oscillations, the hallmark of the well-known AB effect, have been observed with the magnetic field ranging from 0.15 to 2 T [Fig. 9(c)]. Although the perfect periodicity slightly deteriorated at higher fields up to 9 T, the resistance minima has a well defined linear relationship with an approximate period of 0.6 T [Fig. 9(d)]. A weak second harmonic period located at $h/(2e)$ was also observed except for the prominent h/e oscillation period

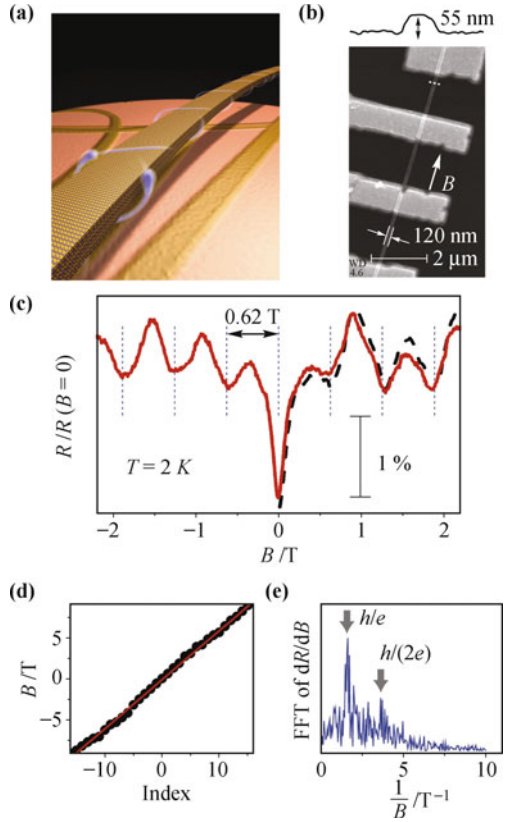

Fig. 9 Transport measurements of Bi_2Se_3 nanoribbons. **(a)** Schematic of Aharonov–Bohm-type quantum interference effects in TI nanoribbon. **(b)** SEM image of a Bi_2Se_3 nanoribbon, 120 nm in width, contacted by four Ti/Au electrodes. The thickness of the nanoribbon was determined by AFM (a line cut in the inset) to be 55 nm. A magnetic field B was applied along the ribbon length. **(c)** Normalized magnetoresistance of the nanoribbon under the magnetic field. A clear modulation of the resistance with a period of 0.62 T is observed, corresponding to one flux quantum (h/e) threaded into the cross section of the nanoribbon. The solid red trace (forward sweep) was taken with a scan rate of 3 mT/sec and the dashed black line (back sweep) at 10 mT/s. **(d)** Magnetic field position of well developed resistance minima. **(e)** Fast Fourier transform (FFT) of the derivative dR/dB in the entire field range. Locations of h/e and $h/(2e)$ flux quantization are labeled. Reproduced from Ref. [13], Copyright © 2010 Nature Publishing Group.

[Fig. 9(e)] in the Bi_2Se_3 nanoribbon by performing FFT of the derivative dR/dB. Most oscillatory features of the AB effect persisted up to 20 K. The transport measurements also revealed that the surface states exist not only on the top and bottom (0001) surfaces but on the side walls of the Bi_2Se_3 nanoribbon as well. The observation of AB oscillations in nanoribbons provides important insights into the topological surface states of Bi_2Se_3 and opens the route for electronic transport experiments in nanostructures of 3D TIs.

The surface states and Fermi level of TI nanostructures can be easily manipulated by an external electric field. Recently, we have observed a clear gate effect and tunable chemical potential in ultrathin Bi_2Te_3 nanoplates by applying a strong electric field from the top gate [17]. In that work, ultrathin Bi_2Te_3 nanoplates grown by VS process on 300 nm SiO_2/Si substrate have an extremely large surface-to-volume ratio and can be electrically gated more effectively than the bulk materials. To enhance the electrical gating effect, a high-k dielectric top gate was deposited onto the individual ultrathin nanoplate. Tunable chemical potentials and pronounced weak antilocalization effect have been observed. Figure 10(a) shows the relationship between the sheet resistance R_S and the top gate voltage V_G measured at 2 K. The R_S showed a quasi-linear increase with negative V_G up to –17.5 V, beyond which the R_S increased more rapidly when the V_G was further increased in the negative direction. The slope of R_S dependence of V_G manifested the sharper increase of R_S beyond –17.5 V [inset of Fig. 10(a)]. The relationship between R_S and V_G suggests that the tunable Fermi level is approaching the bottom of the conduction band at V_G of –17.5 V. The magnetoconductance of the same Bi_2Te_3 nanoplate has been measured with an applied external magnetic field perpendicular to the nanoplate's plane. A weak anti-localization effect characterized by a sharp peak in the magnetoconductance [Fig. 10(b)], resulting from the strong spin–orbit coupling in TI materials, was observed at low magnetic field [13]. More recently, several other groups have

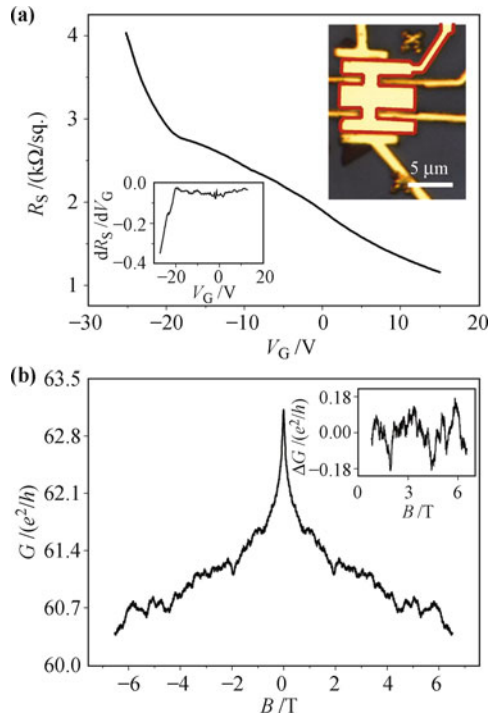

Fig. 10 Transport measurements of Bi_2Te_3 nanoplates. **(a)** Device sheet resistance R_S vs. top gate voltage V_G. R_S increases by ~210% at a negative gate voltage of –25 V. Left inset shows differential resistance over gate voltage that highlights the enhancement of gating response for $V_G < -17.5$ V. Right inset is a typical optical image of a nanoplate device. The top gate is encircled by a red line a visual guide. **(b)** Magnetoconductance in the field range of ±6.5 T. Conductance oscillations (inset) are obtained by subtracting the background. Reproduced from Ref. [17], Copyright © 2010 American Chemical Society.

also reported on the manipulation of surface states of TI nanostructures by external electric fields [15, 16, 18]. For example, Shubnikov–de Haas (SdH) oscillations [15] and surface ambipolar effects [16] have been observed in electric-field-modulated TI nanostructures, which indicate that TI nanostructures provide promising materials for future device applications.

3 Summary

In this mini-review, we have made an overview of recent advances in the controlled synthesis and physical property measurements of nanoscale 3D TI materials. We have succeeded in the controlled growth of quasi-1D nanostructures such as nanowires and narrow nanoribbons via a gold-catalyst-assisted vapor-liquid-solid growth. Beyond, we have achieved the growth of ultrathin nanoplates of Bi_2Se_3 and Bi_2Te_3 with uniform thickness down to one quintuple layer on various substrates via van der Waals epitaxy. We have investigated the evolution of Raman intensity and peak positions with the thickness of TI nanostructures. The strain evolution in few-layer TI nanostructures was studied. We found that the nanoribbons and nanoplates were ideal geometries for direct measurements and manipulation of the topological surface states. Pronounced Aharonov-Bohm-type quantum interference effects were observed in Bi_2Se_3 nanoribbons, providing direct transport evidence of the robust conducting surface states. The surface states of the nanoplates were directly manipulated with a high-k dielectric top gate. Our studies suggest that topological insulator nanostructures hold great promise for the study of topological surface states and future electronic applications.

Acknowledgements We thank Alan Y. Liu for helpful discussions and acknowledge the financial support from the National Natural Science Foundation of China (Grant Nos. 20973007, 20973013, 51072004, 50821061, 20833001, and 11104003), the National Basic Research Program of China (Grant Nos. 2007CB936203, 2011CB921904, and 2011CB933003), and SRF for ROCS, SEM.

References

1. H. J. Zhang, C. X. Liu, X. L. Qi, X. Dai, Z. Fang, and S. C. Zhang, Nat. Phys., 2009, 5: 438
2. J. E. Moore, Nat. Mater., 2010, 464: 194
3. M. Z. Hasan and C. L. Kane, Rev. Mod. Phys., 2010, 82: 3045
4. Y. L. Chen, J. G. Analytis, J. H. Chu, Z. K. Liu, S. K. Mo, X. L. Qi, H. J. Zhang, D. H. Lu, X. Dai, Z. Fang, S. C. Zhang, I. R. Fisher, Z. Hussain, and Z. X. Shen, Science, 2009, 325: 178
5. Y. Xia, D. Qian, D. Hsieh, L. Wray, A. Pal, H. Lin, A. Bansil, D. Grauer, Y. S. Hor, R. J. Cava, and M. Z. Hasan, Nat. Phys., 2009, 5: 398
6. J. G. Checkelsky, Y. S. Hor, M. H. Liu, D. X. Qu, R. J. Cava, and N. P. Ong, Phys. Rev. Lett., 2009, 103: 406601
7. D. Hsieh, Y. Xia, D. Qian, L. Wray, F. Meier, J. H. Dil, J. Osterwalder, L. Patthey, A. V. Fedorov, H. Lin, A. Bansil, D. Grauer, Y. S. Hor, R. J. Cava, and M. Z. Hasan, Phys. Rev. Lett., 2009, 103: 146401
8. A. A. Taskin and Y. Ando, Phys. Rev. B, 2009, 80: 085303
9. J. G. Analytis, J. H. Chu, Y. Chen, F. Corredor, R. D. McDonald, Z. X. Shen, and I. R. Fisher, Phys. Rev. B, 2010, 81: 205407
10. D. Hsieh, D. Qian, L. Wray, Y. Xia, Y. S. Hor, R. J. Cava, and M. Z. Hasan, Nature, 2008, 452: 970
11. Z. Y. Wang, T. Lin, P. Wei, X. F. Liu, R. Dumas, K. Liu, and J. Shi, Appl. Phys. Lett., 2010, 97: 042112
12. Y. Zhang, C. Z. Chang, K. He, L. L. Wang, X. Chen, J. F. Jia, X. C. Ma, and Q. K. Xue, Appl. Phys. Lett., 2010, 97: 194102
13. H. L. Peng, K. J. Lai, D. S. Kong, S. Meister, Y. L. Chen, X. L. Qi, S. C. Zhang, Z. X. Shen, and Y. Cui, Nat. Mater., 2010, 9: 225
14. J. J. Cha, J. R. Williams, D. S. Kong, S. Meister, H. L. Peng, A. J. Bestwick, P. Gallagher, D. Goldhaber-Gordon, and Y. Cui, Nano Lett., 2010, 10: 1076
15. F. X. Xiu, L. A. He, Y. Wang, L. N. Cheng, L. T. Chang, M. R. Lang, G. A. Huang, X. F. Kou, Y. Zhou, X. W. Jiang, Z. G. Chen, J. Zou, A. Shailos, and K. L. Wang, Nat. Nanotechnol., 2011, 6: 216
16. H. Steinberg, D. R. Gardner, Y. S. Lee, and P. Jarillo-Herrero, Nano Lett., 2010, 10: 5032
17. D. S. Kong, W. H. Dang, J. J. Cha, H. Li, S. Meister, H. L. Peng, Z. F. Liu, and Y. Cui, Nano Lett., 2010, 10: 2245
18. J. Chen, H. J. Qin, F. Yang, J. Liu, T. Guan, F. M. Qu, G. H. Zhang, J. R. Shi, X. C. Xie, C. L. Yang, K. H. Wu, Y. Q. Li, and L. Lu, Phys. Rev. Lett., 2010, 105: 4
19. G. H. Zhang, H. J. Qin, J. Chen, X. Y. He, L. Lu, Y. Q. Li, and K. H. Wu, Adv. Funct. Mater., 2011, 21: 2351
20. V. Goyal, D. Teweldebrhan, and A. A. Balandin, Appl. Phys. Lett., 2010, 97: 133117
21. D. Teweldebrhan, V. Goyal, and A. A. Balandin, Nano Lett., 2010, 10: 1209
22. S. S. Hong, W. Kundhikanjana, J. J. Cha, K. J. Lai, D. S. Kong, S. Meister, M. A. Kelly, Z. X. Shen, and Y. Cui, Nano Lett., 2010, 10: 3118
23. J. N. Coleman, M. Lotya, A. O'Neill, S. D. Bergin, P. J. King, U. Khan, K. Young, A. Gaucher, S. De, R. J. Smith, I. V. Shvets, S. K. Arora, G. Stanton, H. Y. Kim, K. Lee, G. T. Kim, G. S. Duesberg, T. Hallam, J. J. Boland, J. J. Wang, J. F. Donegan, J. C. Grunlan, G. Moriarty, A. Shmeliov, R. J. Nicholls, J. M. Perkins, E. M. Grieveson, K. Theuwissen, D. W. McComb, P. D. Nellist, and V. Nicolosi, Science, 2011, 331: 568
24. D. S. Kong, J. C. Randel, H. L. Peng, J. J. Cha, S. Meister, K. J. Lai, Y. L. Chen, Z. X. Shen, H. C. Manoharan, and Y. Cui, Nano Lett., 2010, 10: 329
25. Y. F. Lin, H. W. Chang, S. Y. Lu, and C. W. Liu, J. Phys. Chem. C, 2007, 111: 18538
26. Y. Zhang, K. He, C. Z. Chang, C. L. Song, L. L. Wang, X. Chen, J. F. Jia, Z. Fang, X. Dai, W. Y. Shan, S. Q. Shen,

Q. Niu, X. L. Qi, S. C. Zhang, X. C. Ma, and Q. K. Xue, Nat. Phys., 2010, 6: 584

27. H. W. Liu, H. T. Yuan, N. Fukui, L. Zhang, J. F. Jia, Y. Iwasa, M. W. Chen, T. Hashizume, T. Sakurai, and Q. K. Xue, Cryst. Growth Des., 2010, 10: 4491
28. H. M. Cui, H. Liu, J. Y. Wang, X. Li, F. Han, and R. I. Boughton, J. Cryst. Growth, 2004, 271: 456
29. S. H. Yu, J. Yang, Y. S. Wu, Z. H. Han, J. Lu, Y. Xie, and Y. T. Qian, J. Mater. Chem., 1998, 8: 1949
30. Y. Y. Li, G. A. Wang, X. G. Zhu, M. H. Liu, C. Ye, X. Chen, Y. Y. Wang, K. He, L. L. Wang, X. C. Ma, H. J. Zhang, X. Dai, Z. Fang, X. C. Xie, Y. Liu, X. L. Qi, J. F. Jia, S. C. Zhang, and Q. K. Xue, Adv. Mater. (Deerfield Beach Fla.), 2010, 22: 4002
31. P. Cheng, C. L. Song, T. Zhang, Y. Y. Zhang, Y. L. Wang, J. F. Jia, J. Wang, Y. Y. Wang, B. F. Zhu, X. Chen, X. C. Ma, K. He, L. L. Wang, X. Dai, Z. Fang, X. C. Xie, X. L. Qi, C. X. Liu, S. C. Zhang, and Q. K. Xue, Phys. Rev. Lett., 2010, 105: 076801
32. W. H. Dang, H. L. Peng, H. Li, P. Wang, and Z. F. Liu, Nano Lett., 2010, 10: 2870
33. C. M. Lieber, MRS Bull., 2003, 28: 486
34. P. D. Yang, MRS Bull., 2005, 30: 85
35. P. Gao and Z. L. Wang, J. Phys. Chem. B, 2002, 106: 12653
36. M. T. Bjork, B. J. Ohlsson, T. Sass, A. I. Persson, C. Thelander, M. H. Magnusson, K. Deppert, L. R. Wallenberg, and L. Samuelson, Appl. Phys. Lett., 2002, 80: 1058
37. S. Meister, H. L. Peng, K. McIlwrath, K. Jarausch, X. F. Zhang, and Y. Cui, Nano Lett., 2006, 6: 1514
38. J. S. Lee, S. Brittman, D. Yu, and H. Park, J. Am. Chem. Soc., 2008, 130: 6252
39. H. L. Peng, S. Meister, C. K. Chan, X. F. Zhang, and Y. Cui, Nano Lett., 2006, 7: 199
40. H. L. Peng, C. Xie, D. T. Schoen, and Y. Cui, Nano Lett., 2008, 8: 1511
41. A. Koma, Thin Solid Films, 1992, 216: 72
42. A. Koma, J. Cryst. Growth, 1999, 201: 236
43. H. D. Li, Z. Y. Wang, X. Kan, X. Guo, H. T. He, Z. Wang, J. N. Wang, T. L. Wong, N. Wang, and M. H. Xie, New J. Phys., 2010, 12: 11
44. G. H. Zhang, H. J. Qin, J. Teng, J. D. Guo, Q. L. Guo, X. Dai, Z. Fang, and K. H. Wu, Appl. Phys. Lett., 2009, 95: 053114
45. A. K. Geim and K. S. Novoselov, Nat. Mater., 2007, 6: 183
46. C. Stampfer, S. Fringes, J. Güttinger, F. Molitor, C. Volk, B. Terrés, J. Dauber, S. Engels, S. Schnez, A. Jacobsen, S. Dröscher, T. Ihn, and K. Ensslin, Front. Phys., 2011, 6(3): 271
47. S. Miao, J. Zhu, X. Zhang, and Z. Y. Cheng, Phys. Rev. B, 2001, 65: 052101
48. T. Kehagias, P. Komninou, G. Nouet, P. Ruterana, and T. Karakostas, Phys. Rev. B, 2001, 64: 195329
49. C. L. Song, Y. L. Wang, Y. P. Jiang, Y. Zhang, C. Z. Chang, L. L. Wang, K. He, X. Chen, J. F. Jia, Y. Y. Wang, Z. Fang, X. Dai, X. C. Xie, X. L. Qi, S. C. Zhang, Q. K. Xue, and X. C. Ma, Appl. Phys. Lett., 2010, 97: 143118
50. M. S. Dresselhaus, A. Jorio, M. Hofmann, G. Dresselhaus, and R. Saito, Nano Lett., 2010, 10: 751
51. W. Richter and C. R. Becker, Phys. Status Solidi B, 1977, 84: 619
52. Y. I. Yuzyuk, R. S. Katiyar, V. A. Alyoshin, I. N. Zakharchenko, D. A. Markov, and E. V. Sviridov, Phys. Rev. B, 2003, 68: 104104
53. P. S. Dobal, S. Bhaskar, S. B. Majumder, and R. S. Katiyar, J. Appl. Phys., 1999, 86: 828
54. G. Wedler, C. M. Schneider, A. Trampert, and R. Koch, Phys. Rev. Lett., 2004, 93: 236101
55. A. Fillon, G. Abadias, A. Michel, C. Jaouen, and P. Villechaise, Phys. Rev. Lett., 2010, 104: 096101
56. G. Springholz and K. Wiesauer, Phys. Rev. Lett., 2002, 88: 015507